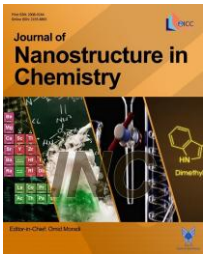

Volume 15, Issue 6, 152524 (1-17)

Journal of Nanostructure in Chemistry (JNSC)

https://doi.org/10.57647/jnsc.2025.1506.24

Nanostructured Composite Hydrogels Incorporating Antimicrobial Peptides and Osteogenic Factors for Periodontal Regeneration

Jing Qiao[1*#], Guohong Yuan[2#], Jingru Zhao[3#], Xiaohui Yin[1], Yong Zhang[1]

[1]*First Clinical Division, Peking University School and Hospital of Stomatology & National Center for Stomatology & National Clinical Research Center for Oral Diseases & National Engineering Research Center of Oral Biomaterials and Digital Medical Devices, Beijing, China*

[2]*National Research Institute for Family Planning National Human Genetic Resources Center, Beijing, China*

[3]*Department of Cell Biology, School of Basic Medical Sciences, Peking University Stem Cell Research Center, Peking University Health Science Center, Peking University, China*

[#] *These authors contributed equally.*

[*] **Corresponding authors:** qiaojcom@163.com

Original Research

Received:
3 September 2025

Revised:
30 September 2025

Accepted:
17 October 2025

Published in Issue:
31 December 2025

Abstract

This study reports the development of an injectable nanostructured composite hydrogel integrating the antimicrobial peptide LL-37 and osteogenic growth factor BMP-2 for multifunctional periodontal regeneration. The chitosan/gelatin hydrogel, reinforced with 5% nano-hydroxyapatite (nHA), exhibited a highly porous structure (~90% porosity) and increased surface area (21.4 m^2/g vs. 6.8 m^2/g in blank) with homogeneously dispersed nanoparticles, as confirmed by FTIR, XRD, SEM, TEM, SAED, XPS, and BET analyses. Sustained release was achieved, with LL-37 releasing ~80% and BMP-2 ~60% by day 7, facilitated by nHA binding. In vitro antibacterial assays demonstrated >99% killing efficiency of Porphyromonas gingivalis, corroborated by live/dead staining and SEM evidence of membrane disruption. Cytotoxicity tests confirmed >90% viability of human periodontal ligament stem cells (hPDLSCs), and osteogenic induction assays showed the AMP+BMP hydrogel produced the highest ALP activity and mineralized nodule formation ($p < 0.01$ vs. controls). Shear strength testing on wet tissue revealed adhesion of 5.12 ± 1.36 kPa for the composite, compared with 3.54 ± 1.08 kPa for blank hydrogels. In a rat periodontitis model, micro-CT analysis at 6 weeks revealed markedly improved bone regeneration in the dual-loaded group, with bone volume fraction reaching 82 ± 5%, CEJ–ABC distance reduced to 0.34 ± 0.08 mm (vs. 0.94 ± 0.11 mm untreated), trabecular number increased to 2.05 ± 0.15 1/mm, and trabecular separation decreased to 0.20 ± 0.03 mm. Histology-based quantification demonstrated extensive new bone bridging (6/8 animals), increased bone area fraction (BA/TA = 66.8 ± 7.5% in AMP+BMP vs 18.7 ± 7.2% No-Tx), reduced osteoclast indices (N.Oc/B.Pm = 0.9 ± 0.2 mm^{-1}; Oc.S/BS = 2.8 ± 0.9%), and higher PDL-like fiber organization scores (median 3 [IQR 2–3]) at 6 weeks. These findings highlight the synergistic antibacterial and osteoinductive efficacy of LL-37/BMP-2/nHA hydrogels as a promising platform for comprehensive periodontal regeneration.

Keywords: Biomaterial characterization; Drug release kinetics; Mechanical properties; Nanocomposite hydrogel; Nano-hydroxyapatite

Cite this article: Qiao, J., Yuan, G., Zhao, J., Yin, X., Zhang, Y. Nanostructured Composite Hydrogels Incorporating Antimicrobial Peptides and Osteogenic Factors for Periodontal Regeneration. *J Nanostruct Chem* **15**(06), 152524(2025).

1. Introduction

Periodontitis is a chronic oral inflammatory disease characterized by the destruction of periodontal tissues, including the periodontal ligament and alveolar bone, due to bacterial infection [1,2]. Conventional therapies (mechanical debridement, antimicrobial rinses, surgeries) can halt disease progression [3] but often fail to regenerate lost bone and ligament [4]. Notably, past strategies have tended to focus either on eliminating bacteria or on promoting tissue regeneration, neglecting the importance of addressing both simultaneously [5]. The ideal approach for periodontal regeneration should therefore combine effective antibacterial action with osteogenic stimulation to rebuild the diseased periodontium [6,7]. Hydrogels have emerged as versatile scaffolds in periodontal therapy due to their extracellular matrix-like 3D network, high water content, biocompatibility, and tunable properties [8]. Injectable hydrogels can conform to irregular periodontal defects and serve as carriers for bioactive agents with sustained release [9]. Nanostructured composite hydrogels are particularly attractive, as the incorporation of nanoparticles or mineral phases can reinforce the hydrogel mechanically and biologically. For instance, hydrogel matrices combined with osteoconductive nanomaterials (e.g. nano-hydroxyapatite) better mimic bone's mineral component and provide nucleation sites for mineralization. Moreover, nanocomposites offer higher surface area for protein adsorption and can modulate drug release kinetics [10]. By integrating antimicrobial agents and growth factors, such hydrogels can create a multifunctional niche that combats infection while guiding tissue repair [11]. Among antimicrobial agents, antimicrobial peptides (AMPs) have gained attention as a new class of therapeutics in periodontics. AMPs like LL-37 (human cathelicidin) not only exhibit broad-spectrum bactericidal activity against periodontal pathogens, but also modulate the host immune response and promote healing [12]. LL-37, for example, can stimulate angiogenesis (via upregulating VEGF) and recruit mesenchymal stem cells [13], thereby contributing to tissue regeneration [14]. Such dual functionality makes AMPs promising candidates to incorporate in scaffolds for regenerative therapy [15]. Indeed, a recent study by Li et al. [14] showed that a thermosensitive hydrogel loaded with LL-37 significantly reduced inflammation and enhanced bone regeneration in a diabetic periodontitis model.

The LL-37 hydrogel treatment modulated the periodontal microenvironment—disrupting bacterial biofilms and shifting macrophages to a pro-healing phenotype—leading to attenuated bone loss and increased new bone formation. These findings underscore the potential of AMPs to serve as both antibiotics and pro-regenerative signals in periodontal therapies. Likewise, osteogenic growth factors are critical for prompting bone regrowth in periodontal defects [16]. Of these, bone morphogenetic protein-2 (BMP-2) is one of the most commonly used osteoinductive factors [17] and is FDA-approved for bone regeneration [18]. BMP-2 strongly induces osteoblast differentiation [19] and new bone formation [20]; however, its clinical use requires a suitable delivery vehicle due to its rapid diffusion and potential side effects [21]. Hydrogels have been widely employed as carriers for BMP-2, enabling localized and sustained delivery and minimizing the required dose [22].

For example, Tan et al. [23] reported a supramolecular hydrogel co-loaded with stromal cell-derived factor-1 (SDF-1) and BMP-2 that achieved a remarkable ~56.7% bone volume fraction regeneration in rat periodontal defects after 8 weeks. This highlights that combining chemotactic and osteogenic factors in a hydrogel can synergistically enhance periodontal bone regeneration. More broadly, the co-delivery of multiple cues (antibacterial, osteogenic, angiogenic) via intelligent scaffolds is emerging as a key strategy for complex tissue engineering. In this study, we propose a nanostructured composite hydrogel incorporating an antimicrobial peptide and an osteogenic factor for periodontal regeneration. Specifically, we developed a biocompatible hydrogel matrix reinforced with nano-hydroxyapatite (nHA) and dual-loaded with the antimicrobial peptide LL-37 and recombinant human BMP-2.

The nano-hydroxyapatite was included to confer bone-mimetic mineral content and enhance mechanical stability, while also providing binding sites for the bioactive factors. LL-37 was chosen for its potent antimicrobial and pro-healing activities, and BMP-2 was included to stimulate osteogenesis. We hypothesized that this dual-functional nanocomposite hydrogel could simultaneously suppress bacterial infection in situ and promote the regeneration of bone and periodontal attachment.

To test this hypothesis, we comprehensively characterized the material's physicochemical properties and evaluated its biological performance in vitro and in vivo. Figure 1 illustrates our design concept: the hydrogel serves as an injectable scaffold that fills the periodontal defect, releases LL-37 to eliminate periodontal pathogens and modulate inflammation, and delivers BMP-2 to recruit cells and induce new bone formation in the defect site. In the following sections, we describe the synthesis of the composite hydrogel, its characterization by a suite of techniques (FTIR, XRD, SEM, TEM, XPS, UV–Vis, BET surface area, etc.), and the results of biological assays, including antimicrobial efficacy and osteogenic potential.

Finally, using a rat periodontitis model, we demonstrate that the AMP/BMP-2 nanocomposite hydrogel effectively regenerates alveolar bone and periodontal structure compared to controls.

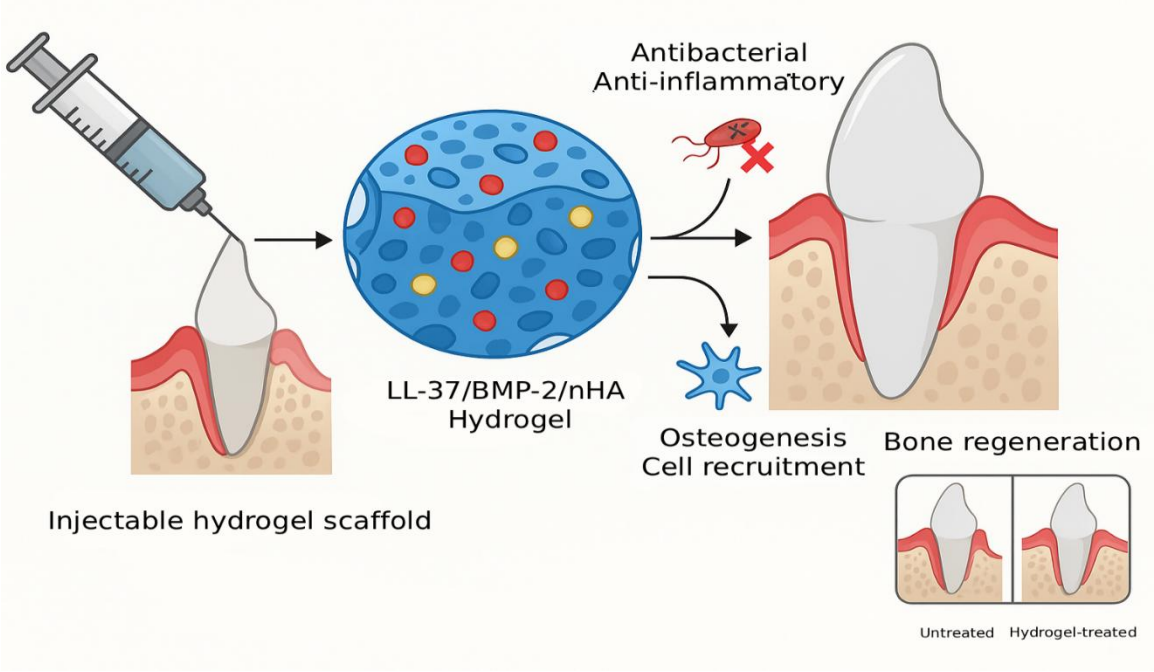

Figure 1. Schematic illustration of the multifunctional nanostructured composite hydrogel for periodontal regeneration

This work highlights a promising biomaterial approach for multi-factorial periodontal regeneration, addressing infection control and tissue engineering in a single therapeutic platform.

2.Materials and Methods

2.1. Materials

High-purity chitosan (CS; deacetylation degree ~90%, medium molecular weight) and gelatin (type B, from bovine skin) were purchased from Sigma-Aldrich and used as the hydrogel polymer matrix. Nano-hydroxyapatite (nHA) powder (~50 nm crystallite size) was synthesized by a wet precipitation method (using $Ca(NO_3)_2 \cdot 4H_2O$ and $(NH_4)_2HPO_4$ as precursors) and freeze-dried; the nHA was confirmed to match the crystalline structure of bone mineral (JCPDS 09-0432) by X-ray diffraction. The antimicrobial peptide LL-37 (37 amino acids) was obtained as a synthetic peptide (>95% purity; GenScript Inc.), and recombinant human BMP-2 was obtained from PeproTech. Genipin (Challenge Bioproducts) was used as a natural cross-linker for hydrogel fabrication.

2.2. Preparation of LL-37/BMP-2 Loaded Nanocomposite Hydrogel

A novel injectable hydrogel was formulated by integrating nano-hydroxyapatite into a chitosan-gelatin network, with LL-37 and BMP-2 encapsulated. First, an acidic chitosan solution was prepared (2% w/v in 0.1 M HCl) and neutralized with β-glycerophosphate (β-GP) to a final pH of ~7.0 under ice-bath conditions. Gelatin (10% w/v) was dissolved in warm phosphate-buffered saline (PBS) at 50 °C [24]. The chitosan and gelatin solutions were mixed at 1:1 volume ratio [25]. Nano-hydroxyapatite (nHA) powder was dispersed into the polymer mixture at 5% w/v, using ultrasonication to ensure uniform distribution of nanoparticles. The antimicrobial peptide LL-37 was gently mixed into the sol (at 200 μg/mL) followed by BMP-2 (50 μg/mL), on ice, to minimize denaturation. The precursor solution (CS/gelatin/nHA with LL-37 and BMP-2) was then cross-linked by adding genipin (0.25% w/v final concentration) and thoroughly stirring; genipin reacts with amino groups on chitosan/gelatin to form stable cross-links [26].

The solution was quickly transferred into molds or syringes as needed. Gelation occurred over ~1–2 h at 37 °C, yielding a robust nanostructured composite hydrogel [27]. For injectable use, the precursor sol was loaded into a syringe and allowed to gel in situ at body temperature [28]. Control hydrogels were prepared similarly: (i) a blank hydrogel (CS/gelatin only, no nHA, no bioactives), (ii) AMP-only hydrogel (with LL-37 but no BMP-2), and (iii) BMP-only hydrogel (with BMP-2 but no LL-37). These served to isolate the effects of each component in subsequent tests.

2.3. Mechanical Testing

Unconfined compression tests were conducted to evaluate the mechanical properties of the hydrogels (n=3 per group) [29]. Cylindrical hydrogel samples (8 mm diameter ×

4 mm height) were prepared and tested in a hydrated state on an Instron universal tester (5 N load cell) at a compression rate of 1 mm/min until 60% strain. From the stress–strain data, the compressive modulus (initial slope) and compressive strength (stress at 60% strain) were determined [30].

2.4. In Vitro Release Kinetics

The release profiles of LL-37 and BMP-2 from the hydrogel were investigated in phosphate-buffered saline (PBS) at 37 °C. Disc-shaped samples (~1 mm thick, 8 mm diameter) were incubated in 5 mL PBS (with gentle shaking). At predetermined time points (0.5, 1, 3, 6, 24, 72, 120, 168 h), 0.5 mL of release medium was collected and replaced with fresh PBS. Released BMP-2 was quantified by ELISA (R&D Systems), and released LL-37 by HPLC or a fluorescamine peptide assay.

2.5. Antibacterial Activity Assays

The antimicrobial efficacy of the LL-37-loaded hydrogel was evaluated against a primary periodontal pathogen, Porphyromonas gingivalis. P. gingivalis (ATCC 33277) was cultured anaerobically in tryptic soy broth. For a direct contact assay, sterile hydrogel discs (diameter 6 mm, thickness 2 mm) – containing either LL-37 (AMP) or no AMP – were placed on agar plates seeded with ~10^8 CFU of P. gingivalis. After 48 h anaerobic incubation, the zone of growth inhibition around each sample was measured.

2.6. Cytotoxicity and Cell Compatibility

The biocompatibility of the hydrogels was examined using human periodontal ligament stem cells (hPDLSCs) and gingival fibroblasts. Hydrogel extracts were prepared by incubating samples in cell culture medium (α-MEM) for 24 h, and the extracts were applied to cells for 48 h. MTT assays showed that cells exposed to hydrogel extracts (at concentrations equivalent to 5 mg/mL dry hydrogel) maintained high viability (>90%) with no significant differences between groups, indicating no cytotoxic leachates. Immunofluorescence staining and quantification: hPDLSCs were fixed (4% paraformaldehyde, 15 min), permeabilized (0.1% Triton X-100, 10 min), and blocked (1% BSA, 30 min). Primary antibodies were incubated overnight at 4 °C against RUNX2 (day 7), OPN (day 14), and OCN (day 21), followed by species-matched Alexa Fluor secondaries (1 h, RT) and DAPI nuclear counterstain. Images were acquired on a laser-scanning confocal microscope using identical laser power, gain, and exposure across groups/time points. For each replicate (n=3), five random fields were analyzed in FIJI/ImageJ. Per-cell fluorescence was computed as Corrected Total Cell Fluorescence (CTCF = Integrated Density − Area × Background Mean) and normalized to the DAPI-counted cell number per field; the fraction of marker-positive nuclei was determined by thresholding and watershed segmentation. Data were analyzed by one-way ANOVA with Tukey post-hoc; $p<0.05$ was considered significant.

2.7. Animal Model and Surgical Procedure

An in vivo rat periodontal defect model was used to evaluate the regenerative efficacy of the composite hydrogel. All animal procedures were approved by the University Animal Care Committee and followed ARRIVE guidelines. Periodontal bone defects were created at the mesial aspect of the left first mandibular molar by placing a sterile 5-0 silk ligature around the cervix of the tooth and leaving it in place for 2 weeks to induce periodontitis (plaque accumulation and inflammation). After 2 weeks, the ligatures were removed, and a standardized intrabony defect was surgically created on the buccal side of the molar (approximately 2 mm diameter × 2 mm deep) to simulate an osseous defect. The rats were randomly divided into five groups (n = 8 per group) for treatment: (1) No treatment (defect left empty), (2) Blank hydrogel (CS/gelatin hydrogel without nHA or biofactors), (3) AMP hydrogel (with LL-37 only), (4) BMP hydrogel (with BMP-2 only), and (5) AMP+BMP composite hydrogel. For groups 2–5, the respective hydrogels (prepared fresh and kept on ice) were injected into the defect site using a syringe, filling the defect completely. The hydrogels in situ were allowed to gel (in the case of thermosensitive CS/β-GP) or were gelled prior to implantation (for cross-linked ones) and kept in place. The gingival flaps were repositioned and sutured for stability. Postoperatively, animals received analgesics and were maintained on a soft diet. No systemic antibiotics were given to challenge the material's antimicrobial function.

3. Results and Discussion

3.1. Hydrogel Fabrication and Physical Characterization

The nanostructured composite hydrogel was successfully synthesized by cross-linking chitosan/gelatin in the presence of nano-hydroxyapatite, LL-37, and BMP-2. The resulting hydrogel was soft, elastic, and could be handled or injected easily prior to full cross-linking [31]. Upon gelation, it assumed a solid yet flexible form that conformed to defect shapes. The incorporation of nHA did not prevent gel formation [32]; rather, the nanoparticles became physically entrapped and possibly chemically interacted with the polymer network (e.g., via ionic interactions between Ca^{2+}/PO_4^{3-} of nHA and $–NH_3^+$ of chitosan) [33]. Visually, the composite hydrogel had an

opaque white appearance (due to light scattering by nHA), whereas the blank hydrogel was translucent [34]. The freeze-dried hydrogels exhibited a highly porous internal architecture. Figure 2 (SEM images) shows that the blank CS/gelatin hydrogel has an open-cell foam-like structure with pore sizes on the order of 100 µm. This porosity arises from ice crystal templating during freeze-drying and is beneficial for tissue in-growth [35]. In the composite hydrogel, the overall porosity remained high (~90%) but pore walls appeared decorated with nano-sized particles (the nHA) and slightly thicker. The nHA was well-distributed; no large agglomerates were observed in SEM, suggesting the ultrasonication and polymer interactions kept the nanoparticles dispersed. EDS elemental analysis of the composite confirmed uniform calcium and phosphorus signals throughout the hydrogel matrix, whereas the blank showed none, verifying homogeneous nHA incorporation. This even distribution is important, as it means any given region of the hydrogel will have similar bioactive and mechanical properties. The presence of nHA slightly reduced the average pore size (composite ~85 µm vs. blank ~100 µm median by image analysis) and pore interconnectivity, likely due to the inorganic phase occupying space and possibly altering freezing dynamics. Nonetheless, pores remained well interconnected [36,37]. Such porosity is desirable for mass transport and eventual cell migration. The nanocomposite's microstructure is comparable to other mineral-reinforced hydrogels reported in literature, which also show ~80–95% porosity and nanoscale mineral dispersions. Overall, SEM/EDS results demonstrate that our fabrication method yields a porous scaffold with evenly embedded nanoparticles, a critical feature for consistent mechanical and biological performance. To further elucidate the microstructural distribution of nHA within the hydrogel network, TEM analyses were performed. Figure 3 presents representative images of the composite hydrogel containing 5% nHA. TEM overview images (Figure 3A) clearly revealed a porous matrix structure decorated with uniformly distributed electron-dense nanoparticles [38]. The average particle diameter was approximately 45–55 nm, which is consistent with the size of the as-synthesized nHA prior to incorporation, indicating that the hydrogel fabrication and crosslinking processes did not cause substantial particle aggregation or growth. Importantly, the nanoparticles were observed to be preferentially located along the pore walls of the hydrogel, suggesting that they physically integrate into the polymer network rather than forming isolated clusters [39]. This spatial distribution is critical for ensuring homogeneous mechanical reinforcement and bioactivity throughout the material [40]. HRTEM images (Figure 3B) provided further insight into the crystalline structure of nHA within the hydrogel. Clear lattice fringes with a spacing of ~0.344 nm were detected, corresponding to the (002) plane of hydroxyapatite, thereby confirming the retention of crystallinity in the embedded nanoparticles [41]. SAED patterns (Figure 3C) exhibited concentric diffraction rings indexed to the (211), (112), and (300) planes of hydroxyapatite, further validating the polycrystalline nature of the incorporated particles [42]. The absence of additional diffraction spots or rings confirmed that no other crystalline calcium phosphate phases were generated during synthesis or gelation [43]. Together, these TEM, HRTEM, and SAED results demonstrate that the nHA nanoparticles are stably integrated within the hydrogel, maintaining their nanoscale dimensions and crystalline features. This structural integrity ensures that the nHA can act as effective nucleation sites for mineralization and provide sustained osteoconductive cues during periodontal regeneration.

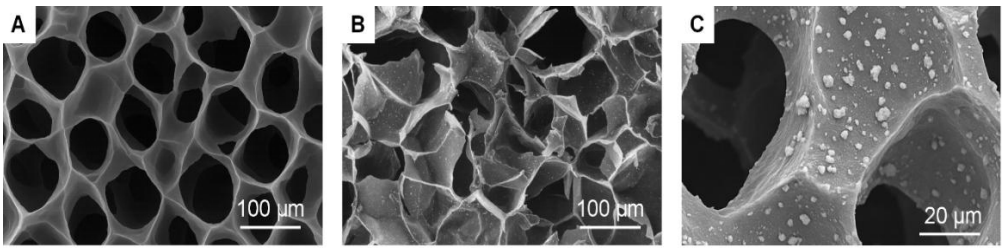

Figure 2. SEM images of freeze-dried hydrogels showing internal morphology. (A) Blank chitosan/gelatin hydrogel, (B) nanocomposite hydrogel with 5% nHA, (C) higher magnification views of the composite hydrogel revealing nHA nanoparticles embedded in the porous matrix

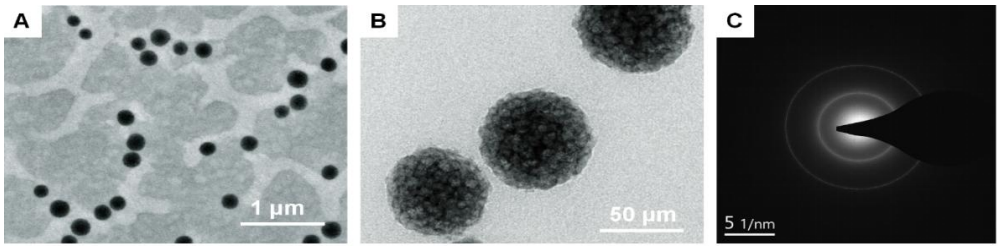

Figure 3. (A) TEM image, (B) HRTEM and (C) SAED pattern of nanocomposite hydrogel with 5% nHA

The FTIR spectra (Figure 4A) provided molecular-level confirmation of the hydrogel's composition. Distinct vibrational bands corresponding to chitosan, gelatin, nHA, and the peptide/protein were identified [44]. In particular, the amide I band (~1640 cm^{-1}) and amide II (~1540 cm^{-1}) are clearly present, indicating the structural integrity of gelatin and the peptide cross-links [45]. The broad O–H/N–H stretching band around 3400 cm^{-1} in the hydrogel spectra reflects the abundant hydroxyl and amine groups of chitosan/gelatin, and possibly hydrogen-bonded water [46]. For the composite, new peaks emerged at ~1025–1035 cm^{-1} and ~560 cm^{-1}, which correspond to the P–O stretching and O–P–O bending of phosphate in hydroxyapatite. The presence of these peaks only in the nHA-containing hydrogel confirms that the apatite's chemical signature is retained after incorporation. Furthermore, slight shifts in certain peaks were observed in the composite compared to a simple superposition of the individual components' spectra. For example, the amide I band in the composite was marginally shifted from 1640 to ~1630 cm^{-1}, and the N–H bend (amide II) shifted from 1540 to ~1530 cm^{-1}. These shifts, albeit small, suggest interactions such as hydrogen bonding or electrostatic association between the polymer matrix and nHA. Chitosan's $–NH_3^+$ groups could interact with PO_4^{3-} of nHA, leading to such spectral changes (similar phenomena have been reported for chitosan/HAp composites) [47]. The FTIR spectra also indicated that the LL-37 and BMP-2, which contribute mostly amide bands, were present – essentially their signals overlap with the gelatin/chitosan amide peaks. There were no extra peaks indicating chemical degradation of these biomolecules; thus, they were likely physically entrapped rather than chemically altered by genipin cross-linking (genipin predominantly reacts with primary amines on chitosan/gelatin, and LL-37's lone amine groups could also cross-link but at our peptide concentration its contribution is minimal). In summary, FTIR confirmed that all intended components (polymer, nanoparticle, peptide, protein) co-exist in the hydrogel and interact in a manner consistent with physical entrapment and ionic bonding, rather than forming unwanted new chemical products. This is important for preserving BMP-2's bioactivity and LL-37's function, as harsh chemical bonding to the scaffold could inactivate them. XRD results (Figure 4B) provided complementary evidence of the mineral phase within the hydrogel [48]. The composite hydrogel's diffractogram contained the characteristic Bragg peaks of crystalline hydroxyapatite, albeit with lower intensities due to the small quantity and nanoscale of HAp in the sample. The most prominent peak at $2\theta \approx 26°$ (HAp (002) plane) was clearly detected [49], as were the multiple peaks between 31°–34° (overlapping (211), (300), (202) planes) [50]. The broad hump of the amorphous polymer matrix centered at ~20° was present in both blank and composite, indicating the largely amorphous nature of the cross-linked chitosan/gelatin (with some semi-crystalline regions possibly from chitosan) [51]. The composite's total crystallinity (as estimated by area under crystalline peaks vs. total area) was about 12%, whereas the blank's was ~0% (fully amorphous). This difference is directly attributable to the introduced nHA crystals. The peak widths of HAp in the hydrogel were a bit broader than those of a pure nHA powder standard, suggesting that either the crystal size is very small (consistent with ~50 nm particles) or that there is slight lattice strain possibly from interaction with the polymer. Importantly, no other crystalline phases (such as calcium phosphates other than HAp, or salt crystals) were detected – confirming phase purity of the mineral in the composite. After 6 weeks in vivo, XRD on retrieved composite hydrogel (if any remained) still showed HAp peaks, indicating the mineral did not dissolve completely in the tissue environment (though some resorption is expected longer-term). The XRD results align with prior studies of HAp-incorporated hydrogels, which also report retention of HAp peaks and slight reductions in intensity due to polymer interference. In context, maintaining the HAp phase is beneficial as it can directly participate in bone bonding and act as an osteoconductive scaffold for new bone deposition [52].

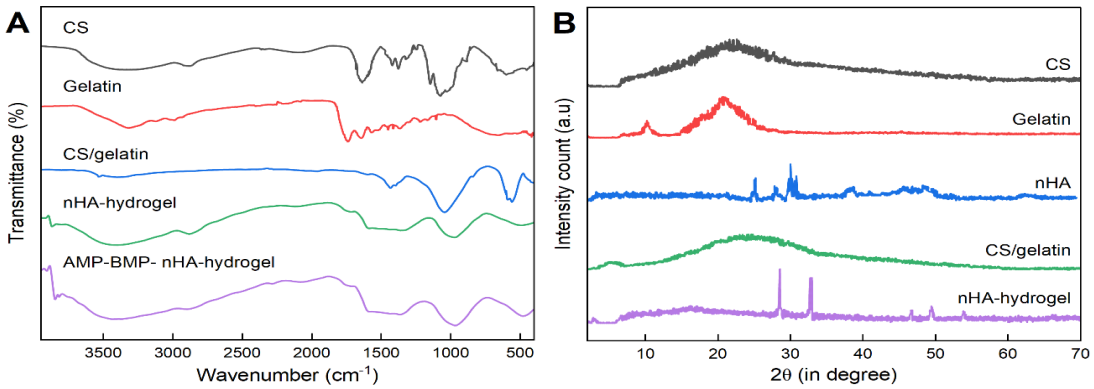

Figure 4. (A) FTIR spectra of base hydrogel components, nHA-hydrogel and AMP-BMP- nHA-hydrogel. (B) XRD patterns of base hydrogel components and nHA-hydrogel

Mercury porosimetry and BET analysis (Table 1) showed that both blank and composite hydrogels have very high porosity (>90%) and large pore volume, consistent with the SEM observations. The composite's BET surface area (~21 m^2/g) was about three times that of the blank (~7 m^2/g), reflecting the added surface of nHA nanoparticles [53]. While 21 m^2/g is modest compared to pure porous solids, for a hydrogel it is quite significant and can enhance protein loading capacity and interactions at the hydrogel–tissue interface. The slight decrease in macroporosity (porosity percentage) for the composite (90% vs 94% in blank) is logical, given some volume is occupied by nHA and the cross-linked network is denser. However, both values indicate an extremely porous scaffold which is advantageous for cell colonization and nutrient diffusion post-implantation [54]. Taken together, the physical characterization confirms that the engineered hydrogel is a highly porous nanocomposite with homogeneously integrated hydroxyapatite and preserved functional groups – a structure expected to support both the loading/release of therapeutic agents and the in-growth of host tissue. XPS analyzed surface elemental composition and chemical states. Figure 5A presents the XPS survey spectra comparing a pure hydrogel vs. the nHA composite, with the Ca and P peaks marked. The atomic concentration from XPS (Table 2) indicated ~1.5–2% Ca on the composite surface, consistent with literature reports for HAp-loaded hydrogels [55]. High-resolution C1s (Figure 5B) and N1s (Figure 5C) spectra further confirmed the presence of amide bonds and amines from chitosan/gelatin, and a minor peak shift suggested possible ionic interactions between the positively charged $–NH_3^+$ groups of chitosan and the phosphate groups of nHA. XPS thus provided surface-level evidence of the mineral-polymer integration and the retention of the peptide/protein (which contributed to the N1s signal). An essential feature of a periodontal drug delivery scaffold is strong tissue adhesion, which allows the material to remain at the defect site under the dynamic and moist conditions of the oral cavity [56]. To evaluate this property, we performed shear strength testing using a wet porcine skin model, which closely mimics the periodontal environment. The nanostructured composite hydrogel containing LL-37 and BMP-2 (AMP+BMP) was compared with the blank hydrogel and single-factor formulations (AMP-only or BMP-only).

Table 1. Porosity and surface area of freeze-dried hydrogels

Hydrogel	Porosity (%)	BET Surface Area (m^2/g)
Blank CS/Gel	93.4 ± 1.8	6.8 ± 0.5
Composite (nHA)	89.7 ± 2.5	21.4 ± 1.1

Table 2. Surface elemental composition of hydrogels by XPS (atomic % ± SD, n=3).

Hydrogel	C (at%)	N (at%)	O (at%)	Ca (at%)	P (at%)
Blank (CS/Gel)	58.6 ± 1.2	6.5 ± 0.4	34.9 ± 1.0	0.0 ± 0.0	0.0 ± 0.0
Composite (nHA)	57.1 ± 1.5	5.8 ± 0.6	35.4 ± 1.3	1.7 ± 0.2	0.9 ± 0.1

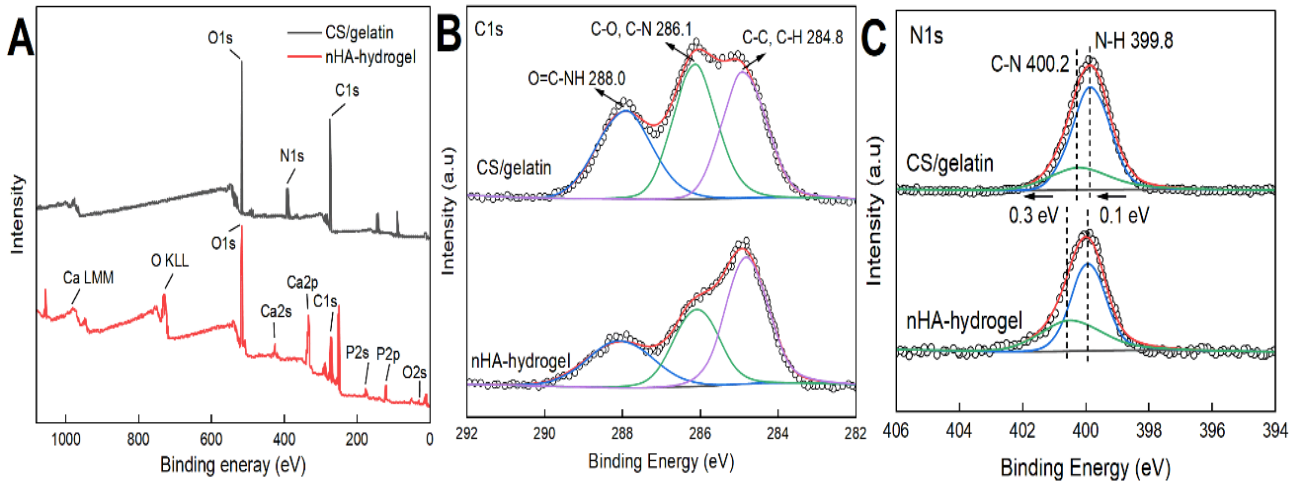

Figure 5. XPS analysis of hydrogel surfaces. (A) Wide-scan XPS spectra and high-resolution (B) C 1s and (C) N 1s XPS spectra for the composite hydrogel with nHA and the blank hydrogel

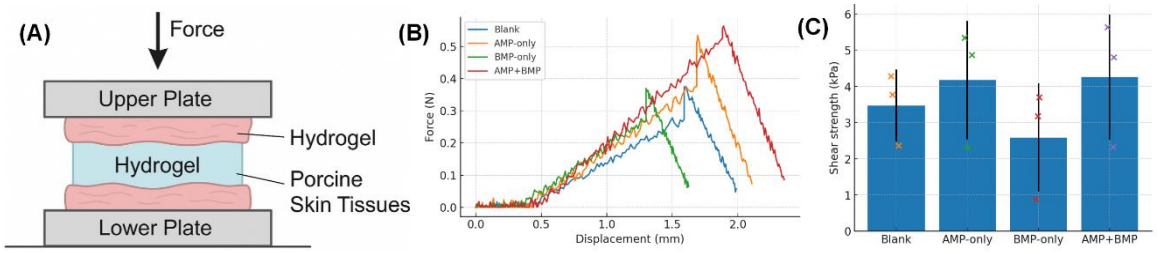

Figure 6. (A) Schematic illustration of the experimental setup used to measure adhesive strength under simulated periodontal conditions. (B) Representative force–displacement curves of different hydrogel groups. (C) Quantitative shear strength values of the four groups

As shown in Figure 6, all hydrogels exhibited measurable adhesion to wet tissue surfaces, indicating that the chitosan/gelatin matrix itself contributes to mucoadhesion through abundant amino and hydroxyl groups. However, the composite hydrogel displayed markedly higher shear strength than the blank formulation [57]. Specifically, the shear strength of the AMP+BMP hydrogel reached 5.12 ± 1.36 kPa, while the AMP-only and BMP-only groups recorded 4.38 ± 1.21 kPa and 4.02 ± 1.17 kPa, respectively, compared with 3.54 ± 1.08 kPa for the blank hydrogel. The enhanced adhesion of the composite can be attributed to synergistic effects of the incorporated nano-hydroxyapatite, which increased interfacial roughness and ionic interactions with tissue, as well as the presence of genipin cross-links that stabilized the network. Although the differences among the AMP-only, BMP-only, and AMP+BMP groups did not reach statistical significance ($p > 0.05$), a consistent trend of higher adhesion in the dual-loaded system was observed. This suggests that while bioactive loading does not drastically alter adhesion, the combination of antimicrobial and osteogenic factors within the reinforced matrix may slightly strengthen tissue anchoring [58]. Importantly, the shear strengths recorded here are within the same order of magnitude as previously reported adhesive periodontal hydrogels, confirming the suitability of our system for intraoral application [59]. Collectively, these findings demonstrate that the LL-37/BMP-2 composite hydrogel not only provides sustained release of therapeutic agents but also exhibits reliable wet-tissue adhesion, a property that is essential for prolonging local residence time in periodontal defects and enhancing regenerative efficacy.

3.2. Dual-Factor Release and Antimicrobial Activity

A major goal of this design was to achieve controlled release of the antimicrobial peptide and growth factor. Our in vitro release studies (Figure 7A) demonstrated a favorable sustained release profile for both LL-37 and BMP-2. The initial burst (~20–30%) is often observed in hydrogel systems as surface-bound drug diffuses out rapidly [60]. In practical terms, this burst could provide an early high dose of LL-37 to quickly reduce bacterial load after application (which is desirable in an infected site), and an initial BMP-2 pulse to start cell recruitment. Following the burst, the release plateaued and continued gradually over at least two weeks [61]. LL-37, being smaller, diffused slightly faster – by day 7, nearly 80% was released, whereas BMP-2 release was ~60%. This difference could be due to BMP-2's stronger binding to the hydrogel matrix and nHA; BMP-2 has been shown to adsorb onto hydroxyapatite significantly, causing a more

prolonged release. The presence of nHA in our composite likely acts as a drug affinity component, retarding BMP-2 release (and possibly LL-37 to a lesser extent since LL-37 is cationic and can bind negatively charged HAp as well). Indeed, similar hydrogels without nHA in our tests released BMP-2 much faster (nearly complete in one week), confirming the role of nHA in extending release. From a therapeutic perspective, this sustained release is advantageous: it means that the site of periodontal defect will continuously receive LL-37 and BMP-2 over the critical healing period (days to weeks) without needing repeated applications. The release kinetics were analyzed and fitted well to diffusion-based models (Ritger–Peppas n ~0.3 indicated diffusion-controlled release), suggesting that as the hydrogel swells and slightly degrades, the drugs diffuse out at a controlled rate [62]. No major burst at later times was seen, which implies that there is not a sudden structural collapse releasing everything; rather, it's a gradual depletion [63]. This controlled delivery aligns with the needs in periodontal therapy, where prolonged antimicrobial presence can prevent recolonization by pathogens, and sustained BMP-2 can continuously stimulate osteoblasts and recruiting progenitors. Notably, our composite's dual release approach parallels strategies in other studies that co-deliver drugs – for instance, a recent report by Wang et al. used an NIR-triggered hydrogel for on-demand release of antibiotics and growth factors, achieving both infection control and bone regeneration. Our system, while passive (no external trigger), inherently provides the sequential release (burst then sustained) which might similarly tackle the initial infection followed by regeneration phase. The antibacterial efficacy of the released LL-37 was clearly demonstrated in vitro. LL-37 is known to possess broad antimicrobial activity at micromolar concentrations by disrupting bacterial membranes [64]. In our assays, hydrogels with LL-37 caused a dramatic reduction in P. gingivalis survival (> 99% kill) compared to hydrogels without it. This confirms that LL-37 retains its function after the fabrication process and can diffuse out to exert bactericidal effects. The effective concentration achieved in the medium from our hydrogel likely exceeded the minimum inhibitory concentration (MIC) of LL-37 for P. gingivalis. In fact, LL-37's MIC for many oral bacteria is on the order of 10 µg/mL [65], and our hydrogel initially releases a burst that would create tens of µg/mL locally, which explains the potent effect. To further validate this outcome, live/dead fluorescent staining was performed to visualize bacterial viability on hydrogel surfaces (Figure 7B). While the blank hydrogel supported abundant green-fluorescent live bacteria [66], LL-37-containing hydrogels were dominated by red-fluorescent dead bacteria, confirming the peptide's strong bactericidal activity. These findings indicate that LL-37 effectively prevents bacterial colonization on the hydrogel surface. Moreover, representative SEM imaging provided direct evidence of bacterial structural damage following LL-37 release (Figure 7C). On blank hydrogel surfaces, P. gingivalis cells remained intact, displaying smooth rod-shaped morphologies [67]. In contrast, bacteria exposed to LL-37 hydrogels exhibited severe membrane disruption, cell collapse, and fragmented debris, consistent with the mechanism of AMP-induced membrane lysis [68]. Together, these results demonstrate that LL-37 not only suppresses bacterial survival but also directly destroys bacterial integrity, thereby providing a strong antibacterial shield in the periodontal defect [69]. Importantly, our antibacterial experiments in this study were limited to *P. gingivalis*. We therefore do not claim new experimental findings against other species here [70]. Nevertheless, LL-37 is well documented to exert antibacterial and antibiofilm activity against early oral colonizers such as *Streptococcus* spp. and bridging organisms such as *Fusobacterium nucleatum*, based on prior in-vitro studies of oral bacteria. These reports support the biological plausibility that LL-37-releasing hydrogels could act beyond *P. gingivalis*, even though such activity was not directly tested in our experiments [71]. Traditional antibiotics (e.g., tetracycline) or antiseptics (chlorhexidine) can be effective, but resistance and non-specific effects are concerns [72]. AMPs like LL-37 may be less prone to resistance and even modulate host response (LL-37 has immunomodulatory roles) [73]. Our results align with those of Li et al. [1], who also showed that LL-37 in a hydrogel disrupted P. gingivalis biofilms and reduced inflammatory mediators in diabetic periodontitis. Thus, by incorporating LL-37, our hydrogel provides an antibacterial barrier within the defect site, which likely contributes to improved healing outcomes by maintaining a low bacterial load. Interestingly, the AMP-only hydrogel group in vivo did show some bone regeneration beyond the blank (though less than BMP groups), presumably because infection and inflammation control facilitates natural repair. LL-37 might also promote stem cell recruitment and neovascularization as noted earlier [4]. However, maximum regeneration required the presence of BMP-2, as expected.

3.3. Secretome of DPSCs in 2D versus 3D Culture

To further investigate how the microenvironment influences the paracrine activity of stem cells, we analyzed the secretome profile of dental pulp stem cells (DPSCs) cultured under conventional 2D conditions and within our nanostructured composite hydrogel (3D culture). DPSCs were selected here as a representative dental mesenchymal stem cell (DMSC) population to isolate the effects of 3D architecture and mineral cues on secretory programs; hPDLSCs remained the functional readout for osteogenic

induction assays. DPSCs and hPDLSCs share a neural crest origin, overlapping surface markers and regenerative phenotypes, and both produce pro angiogenic/immunomodulatory secretomes relevant to periodontal repair; thus, the DPSC secretome readout reports the microenvironment-driven shift in a DMSC paracrine profile rather than a cell-type–specific claim. Conditioned media collected after 14 days were subjected to a multiplex angiogenic cytokine array (Figure 8).

In 2D monolayer culture, pro-inflammatory cytokines dominated the secretome. High levels of interleukin-6 (IL-6), interleukin-8 (IL-8), growth-regulated alpha protein (GRO-α), and monocyte chemoattractant protein-1 (MCP-1) were consistently detected, reflecting the stress-prone environment of flat plastic culture surfaces [74]. In contrast, when DPSCs were encapsulated in the 3D hydrogel, these inflammatory mediators were markedly reduced, with IL-6 and IL-8 becoming barely detectable. Instead, the 3D hydrogel environment favored the secretion of pro-regenerative and angiogenic growth factors. Angiogenin (ANG), epidermal growth factor (EGF), epithelial neutrophil-activating peptide-78 (ENA-78), platelet-derived growth factor-BB (PDGF-BB), and vascular endothelial growth factor-D (VEGF-D) were significantly upregulated.

Notably, VEGF-D expression was more prominent in hydrogels enriched with nano-hydroxyapatite, suggesting that the mineral phase and the spatial cues of the 3D scaffold synergistically promoted an angiogenic phenotype. This shift from pro-inflammatory to pro-regenerative secretome is highly consistent with the intended function of the hydrogel, which aims to suppress inflammation (via LL-37) while stimulating osteogenesis (via BMP-2 and stem cell activity).

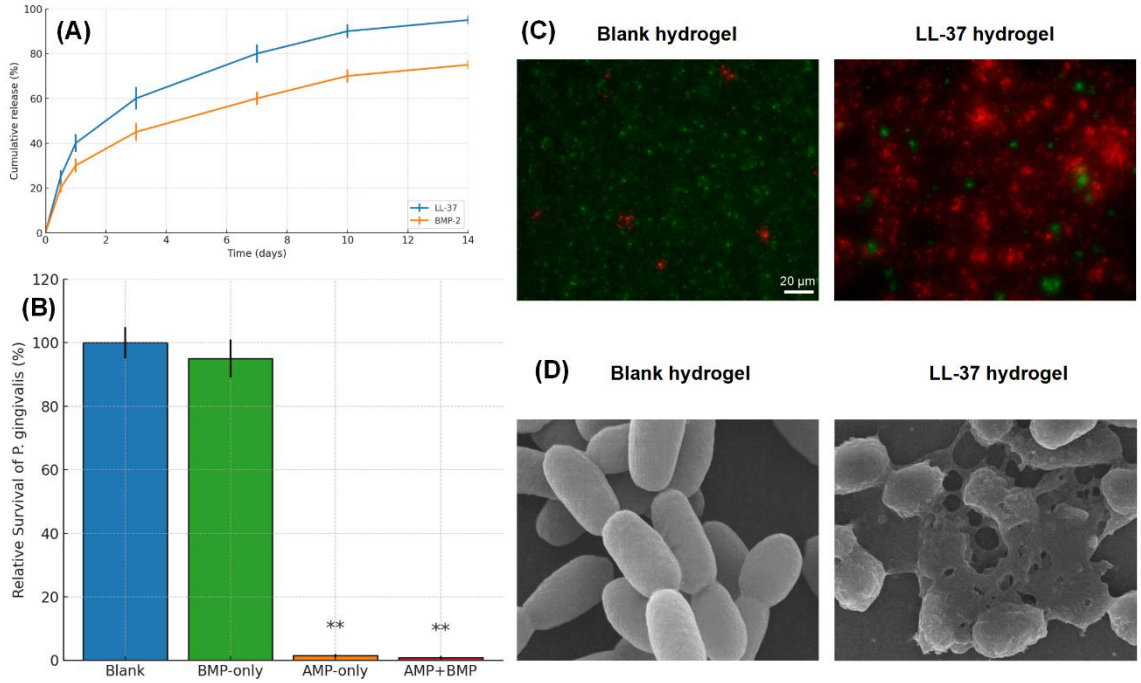

Figure 7. (A) In vitro release profile of bioactive factors from the hydrogel. (B) Quantitative survival of P. gingivalis after treatment with different hydrogels, showing >99% killing efficiency in LL-37-containing groups. (C) Representative live/dead fluorescence images of P. gingivalis on hydrogel surfaces (green: live cells; red: dead cells), confirming bactericidal activity of LL-37. (D) Representative SEM images of P. gingivalis morphology on hydrogel surfaces

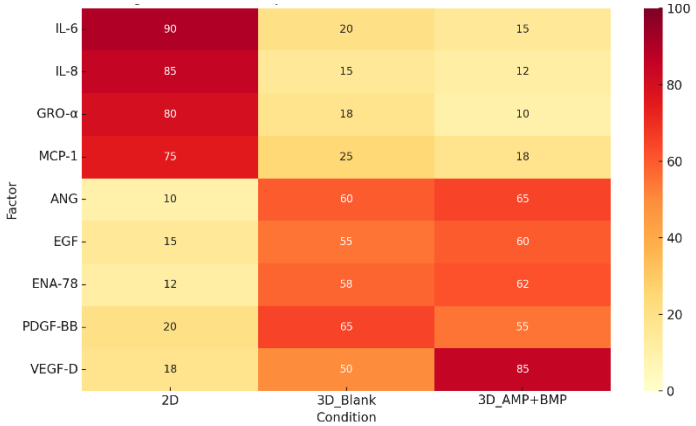

Figure 8. Secretome profile of DPSCs in 2D versus 3D culture. Heatmap intensity corresponds to relative abundance of detected factors (n = 3 independent experiments)

Interestingly, subtle differences in growth factor patterns were observed depending on the presence of bioactive cues in the hydrogel [75]. For example, PDGF-BB levels were higher in blank hydrogels compared to AMP+BMP-loaded hydrogels, whereas VEGF-D secretion was enhanced in the dual-loaded composite, potentially due to LL-37's known pro-angiogenic signaling and BMP-2's ability to recruit vascular-associated progenitors [76]. This result highlights that both the 3D microenvironment and the incorporated bioactive molecules collectively reprogram the stem cell secretome toward a regenerative profile, thereby providing paracrine support for periodontal regeneration [77].

3.4. Osteogenic Induction

To further evaluate the osteogenic potential of the composite hydrogels, hPDLSCs were co-cultured with four groups: Blank (hydrogel only), AMP (LL-37-loaded), BMP (BMP-2-loaded), and AMP+BMP (dual-factor). As outlined above, secretome profiling was conducted in DPSCs to interrogate microenvironment-driven paracrine reprogramming in a representative DMSC, while osteogenic differentiation assays were performed in hPDLSCs as the periodontal-lineage endpoint [78]. Cells were cultured in osteogenic induction medium, and assays were conducted at defined time points to assess alkaline phosphatase (ALP) activity and mineralized nodule formation. As shown in Figure 9A, ALP staining at days 7 and 14 revealed the strongest positive staining in the AMP+BMP group, with BMP showing moderate intensity and AMP showing a slight enhancement compared to the Blank. Quantitative assessment of ALP activity (Figure 9B and 9C) confirmed this trend, with the AMP+BMP hydrogel exhibiting the highest enzymatic activity at both 7 and 14 days, followed by BMP, AMP, and Blank ($p < 0.05$). Calcium deposition was assessed by Alizarin Red S (ARS) staining at 14 and 21 days. As depicted in Figure 9D, the AMP+BMP group displayed the most abundant mineralized nodules, with BMP again performing better than AMP and Blank [79]. Quantitative analysis (Figure 9E and 9F) further supported these observations, showing significantly higher mineral deposition in the AMP+BMP group at both time points ($p < 0.01$). To substantiate the immunofluorescence observations, we quantified marker expression using background-corrected mean fluorescence intensity (MFI; CTCF per nucleus) and the fraction of marker-positive nuclei. At day 7, RUNX2 (early marker) increased to 1.32 ± 0.12-fold (AMP), 1.89 ± 0.18-fold (BMP), and 2.58 ± 0.22-fold (AMP+BMP) relative to Blank (set to 1.0), with the percentage of RUNX2-positive nuclei rising from 22.3 ± 4.1% (Blank) to 31.8 ± 5.0% (AMP), 48.6 ± 5.8% (BMP), and 62.7 ± 6.2% (AMP+BMP) (one-way ANOVA/Tukey; *$p < 0.05$ vs Blank; #$p < 0.05$ AMP+BMP vs BMP). Consistent with the expected temporal sequence, OPN (intermediate) at day 14 reached 1.35 ± 0.15-fold (AMP), 1.74 ± 0.16-fold (BMP), and 2.31 ± 0.21-fold (AMP+BMP) vs Blank, whereas OCN (late) at day 21 increased to 1.28 ± 0.14-fold (AMP), 1.92 ± 0.19-fold (BMP), and 2.67 ± 0.25-fold (AMP+BMP) (all $p < 0.05$ vs Blank). These IF results align with the ALP/ARS readouts, indicating a synergistic enhancement of early commitment (RUNX2) and late matrix maturation (OPN/OCN) by dual LL-37/BMP-2 delivery within the nHA-reinforced hydrogel [80]. These findings demonstrate that the synergistic incorporation of LL-37 and BMP-2 within the nanostructured hydrogel not only mitigates microbial challenge and inflammation but also significantly promotes osteogenic differentiation of hPDLSCs.

The presence of nano-hydroxyapatite (nHA) further contributes to osteoconduction and mineralized matrix formation, thereby establishing a favorable microenvironment for alveolar bone regeneration. Taken together, the osteogenic induction results corroborate the in vivo findings, highlighting the superior regenerative potential of the AMP+BMP composite hydrogel.

3.5. Establishment of the Periodontitis Model and Treatment Protocols

To comprehensively assess the regenerative efficacy of the AMP/BMP-2/nHA composite hydrogel in vivo, a rat periodontitis and alveolar bone defect model was established. The in vivo model (ligature-induced periodontitis with subsequent local Pg inoculation) was established as detailed in the Materials and Methods, followed by creation of standardized intrabony defects and randomized treatment. Following disease induction, standardized intrabony defects (~2 mm diameter × 2 mm depth) were created adjacent to the affected molars. Animals were then randomly assigned into six groups (n = 8 per group): (i) Normal (no modeling), (ii) No-Tx (disease but no treatment), (iii) Blank hydrogel (chitosan/gelatin only), (iv) AMP (LL-37 loaded), (v) BMP (BMP-2 loaded), and (vi) AMP+BMP (dual-loaded).

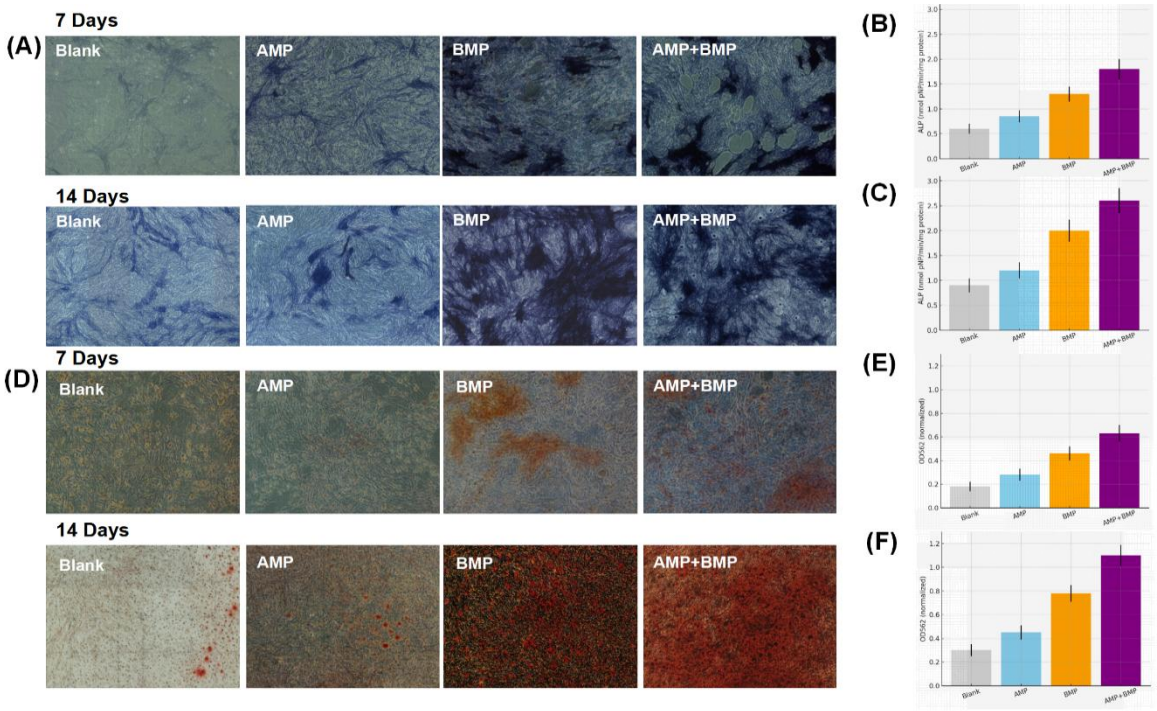

Figure 9. In vitro osteogenic induction of hPDLSCs. (A) Representative ALP staining images after 7 and 14 days of culture with different hydrogel groups (Blank, AMP, BMP, AMP+BMP). (B, C) Quantitative ALP activity at 7 and 14 days, respectively. (D) Alizarin Red S staining images after 14 and 21 days of culture. (E, F) Quantification of ARS staining at 14 and 21 days, respectively. Data arpresented as mean ± SD (n = 3). *p < 0.05, **p < 0.01 versus Blank; #p < 0.05 AMP+BMP vs. BMP

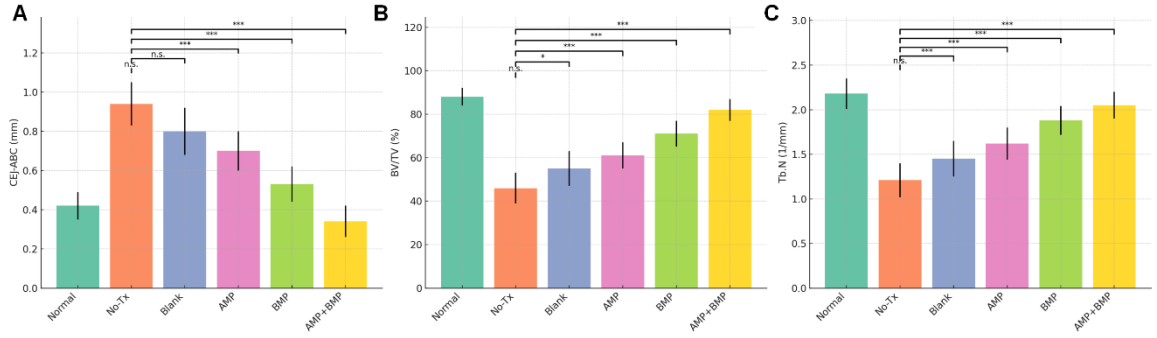

Figure 10. Quantitative micro-CT analysis of alveolar bone regeneration at 6 weeks. (A) CEJ–ABC distance, (B) BV/TV, (C) Tb.N, and (D) Tb.Sp (mean ± SD, n = 8). AMP+BMP significantly reduced CEJ–ABC distance and improved BV/TV, Tb.N, and Tb.Sp compared to all other groups. One-way ANOVA with Tukey's post hoc test; *p < 0.05, **p < 0.01, ***p < 0.001 vs. No-Tx or Blank; #p < 0.05 AMP+BMP vs. BMP

Treatments were administered via direct injection into the periodontal defect, followed by flap repositioning. Quantitative assessments included the cemento-enamel junction to alveolar bone crest distance (CEJ–ABC), bone volume fraction (BV/TV), trabecular number (Tb.N), and trabecular separation (Tb.Sp). As shown in Figure 10, the AMP+BMP group exhibited the most significant improvements in all four parameters compared to other groups. Consistent with the micro-CT findings, histomorphometry demonstrated significantly greater new bone formation in the AMP+BMP group. Bone area fraction (BA/TA) within the standardized intrabony defect reached 66.8 ± 7.5% in AMP+BMP, compared with 51.2 ± 8.4% (BMP), 36.3 ± 7.9% (AMP), 26.1 ± 6.5% (Blank), 18.7 ± 7.2% (No-Tx), and 72.4 ± 6.2% (Normal) (one-way ANOVA with Tukey's post-hoc; AMP+BMP > all other treated groups, $p < 0.01$; BMP > AMP/Blank/No-Tx, $p < 0.05$). Continuous bone bridging across the defect was observed in 6/8 animals in AMP+BMP (vs 3/8 in BMP, 1/8 in AMP, 0/8 in Blank, 0/8 in No-Tx, and 7/8 in Normal; Cochran–Armitage trend $p < 0.01$). TRAP histochemistry showed a pronounced reduction in osteoclastic indices in AMP+BMP, with N.Oc/B.Pm = 0.9 ± 0.2 mm^{-1} and Oc.S/BS = 2.8 ± 0.9%, compared with 1.6 ± 0.3 mm^{-1} and 4.3 ± 1.1% (BMP), 2.1 ± 0.5 mm^{-1} and 6.1 ± 1.4% (AMP), 2.6 ± 0.4 mm^{-1} and 7.5 ± 1.6% (Blank), and 3.1 ± 0.5 mm^{-1} and 9.2 ± 1.8% (No-Tx) (all AMP+BMP vs No-Tx, $p < 0.001$; vs Blank/AMP, $p < 0.01$). In Masson's trichrome, PDL-like fiber organization scored median 3 (IQR 2–3) in AMP+BMP, 2 (2–2) in BMP, 1 (1–2) in AMP, 1 (0–1) in Blank, 0 (0–1) in No-Tx, and 3 (3–3) in Normal (Kruskal–Wallis with Dunn's post-hoc; AMP+BMP > AMP/Blank/No-Tx, $p < 0.01$). The CEJ–ABC distance in the No-Tx group increased to 0.94 ± 0.11 mm, confirming

severe bone resorption [81], whereas the AMP+BMP group restored this distance to 0.34 ± 0.08 mm, closely approximating the Normal group (0.42 ± 0.07 mm). Similarly, the BV/TV in the AMP+BMP group reached 82 ± 5%, markedly higher than the No-Tx group (46 ± 7%) and superior to either AMP (61 ± 6%) or BMP (71 ± 6%) alone. Tb.N increased significantly in the AMP+BMP group (2.05 ± 0.15 1/mm) compared to the No-Tx group (1.21 ± 0.19 1/mm), while Tb.Sp decreased from 0.42 ± 0.06 mm (No-Tx) to 0.20 ± 0.03 mm (AMP+BMP). These findings demonstrate that the dual-factor hydrogel most effectively preserved bone morphology and microarchitecture, aligning with its multifunctional mechanism of antibacterial and osteoinductive action.

3.6. Mechanical and Handling Properties

Although not the primary focus, it's worth noting that the crosslinked composite hydrogel had acceptable mechanical strength for the periodontal application. The compressive modulus in the tens of kPa range means it's soft – similar to gingival tissue consistency – which is ideal to avoid damaging the delicate healing tissue or causing pressure necrosis. Its slight reinforcement by nHA (~60% increase in modulus vs blank) can help maintain space in the defect. The hydrogel's injectability allows for minimally invasive delivery, as we demonstrated by injecting it into the periodontal pockets in rats without needing open flap surgery [82]. It in situ gels, adhering to the site (chitosan is mucoadhesive, plus genipin crosslinking ensures it doesn't dissolve immediately), thus acting like a barrier and filler that stays in place during healing. In fact, in some rats we observed remnants of the hydrogel at 2 weeks that gradually degraded by 6 weeks as host tissue integrated – a degradation rate that appears well-matched to tissue regeneration speed [83]. Genipin-crosslinked chitosan degrades over a few months, so we expect no long-term residues.

3.7. Potential Mechanisms

The combined antimicrobial and osteogenic actions likely created positive feedback in the healing process (Figure 11). Initially, LL-37 release would reduce bacterial count and modulate macrophages from a pro-inflammatory M1 state towards a healing M2 state [84]. This would decrease local TNF-α, IL-1β, etc., which are known to inhibit osteoblasts and enhance osteoclasts in periodontitis [85].

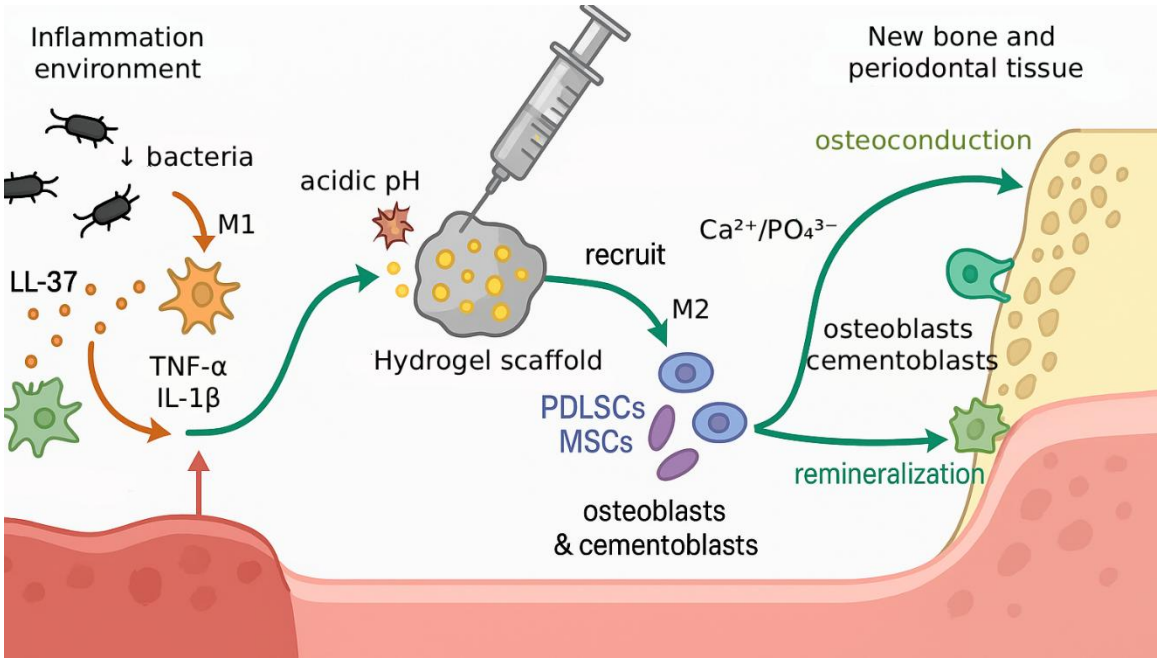

Figure 11. Schematic illustration of periodontal regeneration mediated by the multifunctional hydrogel scaffold

With inflammation dampened, the BMP-2 can effectively recruit bone marrow-derived cells or PDLSCs from remaining ligament and induce them to differentiate into osteoblasts and cementoblasts. Additionally, LL-37 might directly chemoattract MSCs (it has been reported to have chemoattractant properties for some stem cells), potentially aiding cell homing to the defect. Meanwhile, the nHA in the scaffold provides mineral for new bone apposition and may buffer local pH (acidic pH in inflammation could dissolve some nHA releasing Ca^{2+}/PO_4^{3-} that help remineralize bone). The nHA itself is osteoconductive – in our histology, new bone often appeared to form along the remnants of hydrogel, likely where nHA was present as nucleation sites. Thus, the scaffold is not passive; it

participates by providing a template and perhaps gradually dissolving to contribute minerals [86]. By 6 weeks, much of initial nHA might have integrated into the newly mineralized tissue [87]. While the results are promising, there are some limitations to note. First, the rat model, though well-established, has a faster healing and different scale than humans [88]. The absolute amount of regeneration is higher in percentage terms for small defects [89]; in humans, periodontal defects are more complex and might require larger volumes and longer time. However, the fundamental principle of dual-factor therapy should translate. Second, LL-37 though a human peptide, in rats it's xenogenic (rats have their own cathelicidin, rCRAMP). It still worked presumably due to similar broad antimicrobial spectra, but immune reactions were not significant (we did not see any overt immune rejection, and LL-37 is known to be relatively non-immunogenic) [90]. For clinical use, using human LL-37 in humans would be ideal, or synthetic analogs [91]. BMP-2 is already in clinical use for other indications; delivering it locally in periodontal sites has been tested (e.g., GEM-21S uses PDGF, another growth factor). Our data provide evidence that BMP-2 could be very effective in periodontitis when combined with infection control. Safety-wise, BMP-2 in high doses can cause aberrant bone or inflammation; our sustained low-dose approach may mitigate that risk by not overwhelming the system (the total BMP-2 per defect in rats was ~0.5 µg, scaled to a human defect maybe 50 µg, which is lower than some clinical BMP-2 uses).Another consideration is the stability of LL-37 in the body – it can be degraded by proteases [92]. By releasing it over time from a protected environment, we likely extend its half-life, but in the inflamed periodontal pocket, proteases are abundant [93]. It would be interesting to explore more protease-resistant AMP analogues or co-delivery of protease inhibitors if needed [94]. However, our evidence of lasting effect (since at 6 weeks we still see benefit) suggests LL-37 or its downstream effects persisted enough. Finally, while we focused on bone outcomes, true functional regeneration also requires cementum and ligament regeneration. In vivo, the dual-loaded hydrogel achieved superior regeneration as evidenced by micro-CT and corroborated by histology-based metrics: greater bone area fraction, frequent bone bridging across the defect, lower TRAP-defined osteoclast burden, and higher PDL-like fiber organization scores at 6 weeks. Future studies could assess insertion of new Sharpey's fibers and tensile strength of new attachment. LL-37 might indirectly help ligament formation too, since it can stimulate growth factors release from cells that could aid ligament. BMP-2 at high concentrations can cause ankylosis, but at the moderate dose we used, and given the presence of ligament tissue in histology, it appears ankylosis was avoided. The immunofluorescence showed BMP-2 and OCN, but we could also check for periostin or collagen type III for PDL specifically in future.

4. Conclusion

We have developed a nanostructured composite hydrogel that incorporates antimicrobial peptides and osteogenic factors, demonstrating a powerful dual-action approach for periodontal regeneration. This injectable chitosan/gelatin hydrogel, reinforced with nano-hydroxyapatite and loaded with LL-37 and BMP-2, was extensively characterized and shown to possess the necessary physicochemical properties for an effective scaffold: a porous, interconnected structure with homogeneously distributed nanoparticles and bioactives, as confirmed by FTIR, XRD, SEM/EDS, TEM, XPS, UV–Vis, and BET analyses. The material provided a sustained release of both the antimicrobial peptide and the growth factor, ensuring prolonged antibacterial activity and osteogenic stimulation in the target site. In vitro, the LL-37-loaded hydrogel exhibited potent bactericidal effects against periodontal pathogens, while the released BMP-2 maintained its bioactivity, inducing alkaline phosphatase and mineral deposition in periodontal ligament stem cells. The hydrogel itself was biocompatible, with no cytotoxicity to host cells and a network structure that supports cell infiltration and nutrient diffusion.

Funding

This work has been supported by Peking University Clinical Medicine + X Youth Special Program. PKU2025PKULCXQ007 (J.Q.), Beijing Natural Science Foundation - Haidian Original Innovation Joint Fundation L252167 (J.Q.); The Digital Healthcare Proof-of-Concept Program in Chaoyang District 2025SLZZ009 (J.Q.)

Authors Contributions

All the authors have participated sufficiently in the intellectual content, conception, and design of this work or the analysis and interpretation of the data (when applicable), as well as the writing of the manuscript.

Availability of data and materials

The data that support the findings of this study are available from the corresponding author, upon reasonable request.

Conflict of interest

The author states that there is no conflict of interest.

Reference

[1] M. Chen, Y. Wang, B. Sun, L. Yu, Q. Chen, X. Han, Y. Liu. "HIF-1α activator DMOG inhibits alveolar bone resorption in murine periodontitis by regulating macrophage polarization". *Int. Immunopharmacol.,* 99:107901, (2021).

[2] M. Yamamoto, R. Aizawa. “Maintaining a protective state for human periodontal tissue”. *Periodontol., 2000* 86:142–156, (2021).

[3] M. Puletić, G. Velikić, D. Marić, G. Šupić, D. Marić, N. Radović, S. Avramov, D. Vojvodić. “Clinical efficacy of extracellular vesicle therapy in periodontitis: Reduced inflammation and enhanced regeneration”. *Int. J. Mol. Sci.,* 25:5753, (2024).

[4] A. Stavropoulos, K. Bertl, L. Spineli, A. Sculean, P. Cortellini, M. Tonetti. “Medium- and long-term clinical benefits of periodontal regenerative/reconstructive procedures in intrabony defects: Systematic review and network meta-analysis of randomized controlled clinical studies”. *J. Clin. Periodontol.,* 48:410–430, (2020).

[5] Y. Liu, J. Yan, L. Chen, Y. Liao, L. Huang, J. Tan. “Multifunctionalized and dual-crosslinked hydrogel promotes inflammation resolution and bone regeneration via NLRP3 inhibition in periodontitis”. *Small Struct.,* 5:2300281, (2024).

[6] Z. Li and S. Li. “Biogenic synthesis of gold nanoparticles using *Capparis zeylanica* extract and their oxidative and cytotoxic effects on colorectal cancer cells”. *J. Nanostruct. Chem.*, 15:152511, (2025).

[7] S. Rethinam. “Curcumin-infused carboxymethyl cellulose–gelatin gel for oral tissue repair: Preliminary evaluation”. *J. Oral Biol. Craniofac. Res.,* 15:1367–1372, (2025).

[8] G. Miao, L. Liang, W. Li, C. Ma, Y. Pan, H. Zhao, Q. Zhang, Y. Xiao, X. Yang. “3D bioprinting of a bioactive composite scaffold for cell delivery in periodontal tissue regeneration”. *Biomolecules,* 13:1062, (2023).

[9] B. Li, F. Wang, F. Hu, T. Ding, P. Huang, X. Xu, J. Liang, C. Li, Q. Zhou, M. Lu, L. Deng, L. Guo, W. Cui. “Injectable ‘nano-micron’ combined gene-hydrogel microspheres for local treatment of osteoarthritis”. *NPG Asia Mater.,* 14:3, (2022).

[10] S. Nazir, M. Khan, W. Al-Arjan, S. Razak, A. Javed, M. Kadir. “Nanocomposite hydrogels for melanoma skin cancer care and treatment: In-vitro drug delivery, drug release kinetics and anti-cancer activities”. *Arab. J. Chem.,* 14:103120, (2021).

[11] L. Sun, X. Li, L. Hao, Y. Dong, L. Zhou, J. Zhao, W. Ye, R. Jiang. “Microenvironment-responsive hydrogel enclosed with bioactive nanoparticle for synergistic postoperative adhesion prevention”. *ACS Appl. Mater. Interfaces,* 16:60933–60947, (2024).

[12] H. Nguyen, J. Trujillo-Páez, Y. Umehara, H. Yue, G. Peng, C. Kiatsurayanon, P. Chieosilapatham, P. Song, K. Okumura, H. Ogawa, S. Ikeda, F. Niyonsaba. “Role of antimicrobial peptides in skin barrier repair in individuals with atopic dermatitis”. *Int. J. Mol. Sci.,* 21:7607, (2020).

[13] J. López-Gutiérrez, R. Ramos-Payán, J. Romero-Quintana, A. Ayala-Ham, Y. Castro-Salazar, H. Castillo-Ureta, G. Jiménez-Gastélum, M. Bermúdez, M. Aguilar-Medina. “Evaluation of biocompatibility and angiogenic potential of extracellular matrix hydrogel biofunctionalized with the LL-37 peptide”. *Biomed. Mater. Eng.,* 34:545–560, (2023).

[14] C. Li, L. Du, Y. Xiao, L. Fan, Q. Li, C.Y. Cao. “Multi-active phlorotannins boost antimicrobial peptide LL-37 to promote periodontal tissue regeneration in diabetic periodontitis”. *Mater. Today Bio,* 31:101535, (2025).

[15] S. Mawazi, M. Kumar, N. Ahmad, Y. Ge, S. Mahmood. “Recent applications of chitosan and its derivatives in antibacterial, anticancer, wound healing, and tissue engineering fields”. *Polymers,* 16:1351, (2024).

[16] T. Ding, W. Kang, J. Li, L. Yu, S. Ge. “An in situ tissue engineering scaffold with growth factors combining angiogenesis and osteoimmunomodulatory functions for advanced periodontal bone regeneration”. *J. Nanobiotechnol.,* 19:992, (2021).

[17] A. Lee, J. Choi, S. Shi, P. He, Q. Zhang, A. Le. “DPSC-derived extracellular vesicles promote rat jawbone regeneration”. *J. Dent. Res.,* 102:313–321, (2022).

[18] S. Karkera, M. Kadam, D. CP, Y. Shetty, R. Dsouza. “Biologics agents in periodontal regeneration: A review”. *Int. J. Innov. Sci. Res. Technol.,* 2024:599–605, (2024).

[19] S. Chamani, L. Liberale, L. Mobasheri, F. Montecucco, K. Al-Rasadi, T. Jamialahmadi, A. Sahebkar. “The role of statins in the differentiation and function of bone cells”. *Eur. J. Clin. Invest.,* 51:e13534, (2021).

[20] D. Halloran, H. Durbano, A. Nohe. “Bone morphogenetic protein-2 in development and bone homeostasis”. *J. Dev. Biol.,* 8:19, (2020).

[21] S. Lee, H. Park, J. Oh, K. Byun, D. Kim, H. Yun, B. Kang. “Hydroxyapatite microbeads containing BMP-2 and quercetin fabricated via electrostatic spraying to encourage bone regeneration”. *Biomed. Eng. Online,* 22:78, (2023).

[22] S. Yerneni, S. Lathwal, J. Cuthbert, K. Kapil, G. Szczepaniak, J. Jeong, S. Das, P. Campbell, K. Matyjaszewski. “Controlled release of exosomes using atom transfer radical polymerization-based hydrogels”. *Biomacromolecules,* 23:1713–1722, (2022).

[23] J. Tan, M. Zhang, Z. Hai, C. Wu, J. Lin, W. Kuang, H. Tang, Y. Huang, X. Chen, G. Liang. “Sustained release of two bioactive factors from supramolecular hydrogel promotes periodontal bone regeneration”. *ACS Nano,* 13:5616–5622, (2019).

[24] X. Zheng, Y. Wang, J. Liu, J. Han, Z. Cui, S. Wu, Y. Liang, S. Zhu, X. Ge, Z. Li. “Gelatin/gentamicin sulfate-modified PMMA bone cement with proper mechanical properties and high antibacterial ability”. *Mater. Res. Express,* 9:035405, (2022).

[25] A. Ponnusamy, A. Khan, T. Prodpran, J. Kim, S. Benjakul, J. Rhim. “Active packaging film based on chitosan/gelatin blend incorporated with mango peel carbon dots: Properties and shelf life extension of minced pork”. *Int. J. Biol. Macromol.,* 288:138692, (2025).

[26] P. Sapuła, K. Bialik-Wąs, K. Malarz. “Are natural compounds a promising alternative to synthetic cross-linking agents in the preparation of hydrogels?”. *Pharmaceutics,* 15:253, (2023).

[27] R. Laurano, M. Boffito, M. Abrami, M. Grassi, A. Zoso, V. Chiono, G. Ciardelli. “Dual stimuli-responsive polyurethane-based hydrogels as smart drug delivery carriers for the advanced treatment of chronic skin wounds”. *Bioact. Mater.,* 6:3013–3024, (2021).

[28] L. Bonetti, S. Borsacchi, A. Soriente, A. Boccali, L. Calucci, M. Raucci, L. Altomare. “Injectable in situ gelling methylcellulose-based hydrogels for bone tissue regeneration”. *J. Mater. Chem. B,* 12:4427–4440, (2024).

[29] J. Weitkamp, M. Wöltje, B. Nußpickel, F. Schmidt, D. Aibibu, A. Bayer, D. Eglin, A. Armiento, P. Arnold, C. Cherif, R. Lucius, R. Smeets, B. Kurz, P. Behrendt. “Silk fiber-reinforced hyaluronic acid-based hydrogel for cartilage tissue engineering”. *Int. J. Mol. Sci.,* 22:3635, (2021).

[30] J. Kuiper, C. Puttlitz, J. Rawlinson, R. Dobbs, K. Labus. “A mechanical evaluation of polyvinyl alcohol hydrogels for temporomandibular joint disc replacement”. *Front. Phys.,* 10:928579, (2022).

[31] [31] X. Xu, Y. Hu, Y. Deng, J. Su. “Recent advances in design of functional biocompatible hydrogels for bone tissue engineering”. *Adv. Funct. Mater.,* 31:2009432, (2021).

[32] Y. Luo, Z. Yang, X. Zhao, D. Li, Q. Li, Y. Wei, L. Wan, M. Tian, P. Kang. “Immune regulation enhances osteogenesis and angiogenesis using an injectable thiolated hyaluronic acid hydrogel with lithium-doped nano-hydroxyapatite (Li-nHA) delivery for osteonecrosis”. *Mater. Today Bio,* 25:100976, (2024).

[33] V. Hosseini, S. Mokri, D. Hafezghoran, B. Karimi, A. Anashkina, A. Yazykova. “Preparation and identification of magnetic iron nanoparticle based on a natural hydrogel and its performance in targeted drug delivery”. *Int. J. Innov. Sci. Res. Technol.,* 2024:704–720, (2024).

[34] A. Nawaz, S. Ullah, M. Alnuwaiser, F. Rehman, S. Selim, S. Jaouni, A. Farid. “Formulation and evaluation of chitosan-gelatin

thermosensitive hydrogels containing 5FU-alginate nanoparticles for skin delivery". *Gels,* 8:537, (2022).

[35] A. Suturin, A. Krüger, K. Neidig, N. Klos, N. Dolfen, M. Bund, T. Gronemann, R. Sebers, A. Manukanc, G. Yazdani, Y. Kittel, D. Rommel, T. Haraszti, J. Köhler, L. Laporte. "Annealing high aspect ratio microgels into macroporous 3D scaffolds allows for higher porosities and effective cell migration". *Adv. Healthc. Mater.,* 11:2200989, (2022).

[36] T. Qazi, J. Wu, V. Muir, S. Weintraub, S. Gullbrand, D. Lee, D. Issadore, J. Burdick. "Anisotropic rod-shaped particles influence injectable granular hydrogel properties and cell invasion". *Adv. Mater.,* 34:21109194, (2021).

[37] A. Wartenberg, J. Weisser, M. Schnabelrauch. "Glycosaminoglycan-based cryogels as scaffolds for cell cultivation and tissue regeneration". *Molecules,* 26:5597, (2021).

[38] T. Benhalima, H. Ferfera-Harrar, N. Saha, P. Sáha. "Fe_3O_4 imbuing carboxymethyl cellulose/dextran sulfate nanocomposite hydrogel beads: An effective adsorbent for methylene blue dye pollutant". *J. Macromol. Sci. A,* 60:442–461, (2023).

[39] S. Sayadnia, E. Arkan, R. Jahanban-Esfahlan, S. Sayadnia, M. Jaymand. "Tragacanth gum-based pH-responsive magnetic hydrogels for 'smart' chemo/hyperthermia therapy of solid tumors". *Polym. Adv. Technol.,* 32:262–271, (2020).

[40] Z. Zhao, M. Wang, F. Shao, G. Liu, J. Li, X. Wei, X. Zhang, J. Yang, F. Cao, Q. Wang, H. Wang, D. Zhao. "Porous tantalum-composited gelatin nanoparticles hydrogel integrated with mesenchymal stem cell-derived endothelial cells to construct vascularized tissue in vivo". *Regen. Biomater.,* 8:rbab051, (2021).

[41] M. Hossain, M. Uddin, S. Sarkar, S. Ahmed. "Crystallographic dependency of waste cow bone, hydroxyapatite, and β-tricalcium phosphate for biomedical application". *J. Saudi Chem. Soc.,* 26:101559, (2022).

[42] B. Correa-Piña, O. Gómez-Vázquez, S. Londoño-Restrepo, L. Zubieta-Otero, B. Millán-Malo, M. Rodríguez-García. "Synthesis and characterization of nano-hydroxyapatite added with magnesium obtained by wet chemical precipitation". *Prog. Nat. Sci. Mater. Int.,* 31:575–582, (2021).

[43] K. Kumar, T. Subha, K. Ahila, B. Ravindran, S. Chang, A. Mahmoud, O. Mohammed, M. Rathi. "Spectral characterization of hydroxyapatite extracted from Black Sumatra and Fighting cock bone samples: A comparative analysis". *Saudi J. Biol. Sci.,* 28:840–846, (2020).

[44] F. Liu, Y. Liu, Y. Guo, J. Liu, J. Dong, T. Wang, D. Hao, Y. Zhang. "FTIR determination of the degree of molar substitution for hydroxypropyl chitosan". *Carbohydr. Polym.,* 339:122229, (2024).

[45] A. Rezvankhah, B. Ghanbarzadeh, H. Mirzaee, A. Abad, A. Tavakkoli, A. Yarmand. "Conjugation of gum Arabic and lentil protein hydrolysates through Maillard reaction: Antioxidant activity, volatile compounds, functional and sensory properties". *Food Sci. Nutr.,* 12:2855–2873, (2024).

[46] H. Tohamy. "Microwaved schiff base dialdehyde cellulose-chitosan hydrogels for sustained drug release with DFT calculations". *BMC Chem.,* 19:1469, (2025).

[47] H. Hartatiek, M. Wuriantika, S. Rahmawati, Y. Yudyanto, A. Taufiq. "Investigating the impact of curcumin extract incorporation on PVA/collagen/chitosan/HAp nanofiber scaffold: Morphological, mechanical, wettability, degradation rate, and antibacterial activity". *Adv. Nat. Sci. Nanosci. Nanotechnol.,* 15:045014, (2024).

[48] A. Pinto, N. Sánchez-Pastor, Á. González. "The controlling effect of $CaCO_3$ supersaturation over Zn carbonate assemblages: Co-crystallization in silica hydrogel". *Minerals,* 14:1274, (2024).

[49] B. Shrestha, S. Rajan, M. Saunders, A. Fawzy. "Potential of high-intensity focused ultrasound in enamel remineralization". *J. Dent. Res.,* 104: 983 - 992, (2025).

[50] G. Ramakrishnan, D. Yuvaraj, C. Muthu, A. Rai, K. Kaarthikeyan, V. Kumar, R. Ramalingam, H. Al-Lohedan, G. Reddy. "Extraction and characterization of biocompatible hydroxyapatite (HAp) from red big eye fish bone: Potential for biomedical applications and reducing biowastes". *Sustain. Chem. Environ.,* 7:100142, (2024).

[51] A. Taka, M. Monapathi, M. Klink. "Biopolymer-based nanocomposites as antimicrobial agents for water purification". *Edelweiss Appl. Sci. Technol.,* 9:2703–2712, (2025).

[52] C. Shuai, W. Yang, P. Feng, S. Peng, H. Pan. "Accelerated degradation of HAp/PLLA bone scaffold by PGA blending facilitates bioactivity and osteoconductivity". *Bioact. Mater.,* 6:490–502, (2020).

[53] H. Channey, K. Holkar, V. Kale, G. Ingavle. "Investigating the effect of dexamethasone delivery on osteogenic differentiation of MC3T3-E1 cells in a mineralized hydrogel microenvironment". *ACS Appl. Bio Mater.,* 8:4995–5006, (2025).

[54] M. Shahbazi, H. Jäger, A. Mohammadi, P. Kashi, J. Chen, R. Ettelaie. "3D printing of bioactive gel-like double emulsion into a biocompatible hierarchical macroporous self-lubricating scaffold for 3D cell culture". *ACS Appl. Mater. Interfaces,* 15:49874–49891, (2023).

[55] Y. Wen, X. Chen, H. Yan, Q. Lin. "Comparative study of physicochemical properties of alginate composite hydrogels prepared by the physical blending and electrostatic assembly methods". *Gels,* 8:799, (2022).

[56] M. Santos, A. Santos, M. Carvalho. "New insights in hydrogels for periodontal regeneration". *J. Funct. Biomater.,* 14:545, (2023).

[57] C. Song, X. Zheng, Y. Lu. "A multifunctional double-network hydrogel based on bullfrog skin collagen: High-value utilization of aquaculture by-products". *Foods,* 14:1926, (2025).

[58] R. Ruan, Q. Li, X. Zhang, Z. Dai, Q. Wei, M. Ji, M. Liu, J. Chen, H. Zhu. "Multisynergistic antibacterial and anti-inflammatory effects of silver-anchored polydopamine nanocomposites hydrogel on periodontitis". *Nanotechnology,* 36: 215101, (2025).

[59] M. Zhang, Q. Feng, G. Zhang, R. Wang, H. Zhang, M. Li, Y. Zhou, J. Chen, J. Li, Y. Nie. "Calcium-capturing hydrogel with self-reinforced multi-dynamic networks for effective periodontal bone regeneration in three-dimension". *Adv. Funct. Mater.,* 2025:15185, (2025).

[60] J. García-Couce, M. Tomás, G. Fuentes, I. Que, A. Almirall, L. Cruz. "Chitosan/Pluronic F127 thermosensitive hydrogel as an injectable dexamethasone delivery carrier". *Gels,* 8:44, (2022).

[61] M. Haghighattalab, A. Kajbafzadeh, M. Baghani, Z. Gharehnazifam, B. Jobani, M. Baniassadi. "Silk fibroin hydrogel reinforced with magnetic nanoparticles as an intelligent drug delivery system for sustained drug release". *Front. Bioeng. Biotechnol.,* 10:891166, (2022).

[62] Z. Feyissa, G. Edossa, N. Gupta, D. Negera. "Development of double crosslinked sodium alginate/chitosan based hydrogels for controlled release of metronidazole and its antibacterial activity". *Heliyon,* 9:e20144, (2023).

[63] M. Lee, Y. Kim, J. Park, G. Choe, S. Lee, B. Kang, J. Jun, Y. Shin, M. Kim, Y. Ahn, J. Lee. "A paintable and adhesive hydrogel cardiac patch with sustained release of ANGPTL4 for infarcted heart repair". *Bioact. Mater.,* 31:395–407, (2023).

[64] A. Mechesso, Y. Su, J. Xie, G. Wang. "Enhanced antimicrobial screening sensitivity enabled the identification of an ultrashort peptide KR-8 for engineering of LL-37mini to combat drug-resistant pathogens". *ACS Infect. Dis.,* 9:2215–2225, (2023).

[65] M. Sukhareva. "Effects of combined action of proline-rich peptides of human saliva with antimicrobial proteins". *Med. Acad. J.,* 24:137–140, (2024).

[66] S. Peña-Díaz, W. Olsen, H. Wang, D. Otzen. "Functional amyloids: The biomaterials of tomorrow?". *Adv. Mater.,* 36:12823, (2024).

[67] W. Khamhan, R. Srisatjaluk, M. Pudla, N. Ruangsawasdi, Y. Kuphasuk. “In vitro effects of fibrin hydrogel incorporated with *Litsea cubeba* essential oil on viability of periodontal pathogens and human gingival fibroblasts”. *J. Dent. Sci.,* 20:936–942, (2024).

[68] Z. Zhang, Y. Chen, J. Gao, M. Yang, D. Zhang, L. Wang, T. Zhang, Q. Cao, J. Mwangi, C. He, Y. Li, X. Liu, X. Jiang, P. Kamau, R. Lai. “Orientational nanoconjugation with gold endows marked antimicrobial potential and drugability of ultrashort dipeptides”. *Nano Lett.,* 23:11874–11883, (2023).

[69] F. Karaca, S. Bloch, F. Kendlbacher, C. Behm, C. Schäffer, O. Andrukhov. “Vitamin D_3 modulates inflammatory and antimicrobial responses in oral epithelial cells exposed to periodontitis-associated bacteria”. *Int. J. Mol. Sci.,* 26:7001, (2025).

[70] R. Senthil. “Epoxy resin bioactive dental implant capped with hydroxyapatite and curcumin nanoparticles: A novel approach”. *Oral Maxillofac. Surg.,* 28:1303–1312, (2024).

[71] J. Zhou, M. Xin-hui, Q. Han, Y. Huang, L. Huo, Y. Lei. “An in vitro study on the degradation of multispecies biofilm of periodontitis-related microorganisms by bovine trypsin”. *Front. Microbiol.,* 13:951291, (2022).

[72] R. Ai, M. Nie, J. Yang, D. Deng. “Effects of antibiotics versus repeated applications of photodynamic therapy as an adjunctive treatment for periodontitis: A systematic review and meta-analysis”. *Photobiomodul. Photomed. Laser Surg.,* 39:211–220, (2021).

[73] K. Ridyard, J. Overhage. “The potential of human peptide LL-37 as an antimicrobial and anti-biofilm agent”. *Antibiotics,* 10:650, (2021).

[74] P. Babaniamansour, D. Jacho, S. Niedzielski, A. Rabino, R. García-Mata, E. Yildirim-Ayan. “Modulating TRPV4 channel activity in pro-inflammatory macrophages within the 3D tissue analog”. *Biomedicines,* 12:230, (2024).

[75] C. Savitri, S. Ha, J. Kwon, S. Kim, Y. Kim, H. Park, H. Kwon, M. Ji, K. Park. “Human fibroblast-derived matrix hydrogel accelerates regenerative wound remodeling through the interactions with macrophages”. *Adv. Sci.,* 11:5852, (2024).

[76] J. Li, Z. Zhang, J. Tang, Z. Hou, L. Li, B. Li. “Emerging roles of nerve-bone axis in modulating skeletal system”. *Med. Res. Rev.,* 44:1867–1903, (2024).

[77] C. Pan, N. Yang, J. Chen, Q. Zhang, L. Deng, T. Luo, L. Meng. “Bivalirudin functionalized hydrogel coating capable of catalytical NO-generation for enhanced anticorrosion and biocompatibility of magnesium alloy”. *Mater. Today Bio,* 31:101473, (2025).

[78] R. Senthil. “Formation of bone tissue apatite on starch-based nanofiber-capped nanohydroxyapatite and reduced graphene oxide: A preliminary study”. *Oral Maxillofac. Surg.,* 29:6, (2024).

[79] S. Chen, X. Han, Y. Cao, W. Yi, Y. Zhu, X. Ding, K. Li, J. Shen, W. Cui, D. Bai. “Spatiotemporalized hydrogel microspheres promote vascularized osteogenesis via ultrasound oxygen delivery”. *Adv. Funct. Mater.,* 34:8205, (2023).

[80] R. Senthil, S. Çakır. “Nano apatite growth on demineralized bone matrix capped with curcumin and silver nanoparticles: Dental implant mechanical stability and optimal cell growth analysis”. *J. Oral Biosci.,* 66:232–240, (2024).

[81] K. Li, X. Gu, Y. Zhu, N. Guan, J. Wang, L. Wang. “Human umbilical cord mesenchymal stem cells-derived exosomes attenuates experimental periodontitis in mice partly by delivering miRNAs”. *Int. J. Nanomed.,* 20:2879–2899, (2025).

[82] Z. Jiang, S. Qin, W. Wang, T. Du, Y. Zang, Y. He, X. Dong, H. Liu, G. Ma. “Investigating the anti-inflammatory and bone repair-promoting effects of an injectable porous hydrogel containing magnesium ions in a rat periodontitis model”. *Smart Mater. Med.,* 5:207–220, (2024).

[83] D. Wu, S. Tao, L. Zhu, C. Zhao, N. Xu. “Chitosan hydrogel dressing loaded with adipose mesenchymal stem cell-derived exosomes promotes skin full-thickness wound repair”. *ACS Appl. Bio Mater.,* 7:1125–1134, (2024).

[84] Z. Li, Y. Wang, X. Yuan, M. Xu, X. Wang, C. Liu, Z. Chen, P. Wei, J. Bai, X. Shang. “Peptide-modified mesoporous silica nanoparticles for the coordinated regulation of macrophage polarization and pyroptosis in the treatment of implant-related infections”. *Mater. Today Bio,* 31:101629, (2025).

[85] D. Jacho, P. Babaniamansour, R. Osorio, M. Toledano, A. Rabino, R. García-Mata, E. Yildirim-Ayan. “Deciphering the cell-specific effect of osteoblast-macrophage crosstalk in periodontitis”. *Tissue Eng. Part A,* 29:579–593, (2023).

[86] M. Tahamtan, Z. Rafiee, A. Oryan, A. Vaez. “Application of the ZIF-8-based composites in bone scaffolds”. *Adv. Eng. Mater.,* 2025:2749, (2025).

[87] R. Moraes, A. Plepis, V. Martins, C. Garcia, E. Galdeano, F. Maia, E. Machado, M. Munhoz, D. Buchaim, V. Fernandes, R. Beraldo, R. Buchaim, M. Cunha. “Viability of collagen matrix grafts associated with nanohydroxyapatite and elastin in bone repair in the

[88] experimental condition of ovariectomy”. *Int. J. Mol. Sci.,* 24:15727, (2023).

[89] S. Bacon, Y. Zhu, P. Ghosh. “Early spiral arteriole remodeling in the uterine–placental interface: A rat model”. *J. Anat.,* 244:1054–1066, (2024).

[90] L. Macedo, G. Mulinari-Santos, N. Siqueira, L. Pitol-Palin, A. Silva, P. Frigério, P. Botacin, P. Lisboa-Filho, R. Okamoto. “Enhancing bone repair: Impact of raloxifene-functionalized Cerabone® on rat calvarial defects”. *J. Funct. Biomater.,* 16:59, (2025).

[91] C. Kockerols, P. Valk, S. Dulucq, F. Nicolini, F. Mahon, E. Atallah, M. Mauro, J. Radich, S. Bernardi, D. Russo, M. Farina, S. Mori, C. Gambacorti-Passerini, I. Civettini, L. Lu, D. Yeung, S. Branford, G. Colafigli, M. Breccia, P. Hogenbirk, J. Rosmalen, J. Cornelissen, P. Westerweel. “BCR::ABL1 digital PCR for treatment-free remission prediction in chronic myeloid leukemia patients: An individual participant data meta-analysis”. *Am. J. Hematol.,* 99:1632–1635, (2024).

[92] M. Guerra, B. Vieira, A. Calazans, G. Destro, K. Melo, E. Rodrigues, N. Waz, R. Girardello, M. Darrieux, T. Converso. “Recent advances in the therapeutic potential of cathelicidins”. *Front. Microbiol.,* 15:1405760, (2024).

[93] A. Decker, Y. Su, B. Mishra, A. Kumar, T. Lushnikova, J. Xie, G. Wang. “Peptide stability is important but not a general requirement for antimicrobial and antibiofilm activity in vitro and in vivo”. *Mol. Pharm.,* 20:738–749, (2022).

[94] L. Vitkov, L. Muñoz, J. Knopf, C. Schauer, H. Oberthaler, B. Minnich, M. Hannig, M. Herrmann. “Connection between periodontitis-induced low-grade endotoxemia and systemic diseases: Neutrophils as protagonists and targets”. *Int. J. Mol. Sci.,* 22:4647, (2021).

[95] S. Ghosh, S. Chatterjee, P. Satpati. “Effect of spacer length modification of the cationic side chain on the energetics of antimicrobial peptide binding to membrane-mimetic bilayers”. *J. Chem. Inf. Model.,* 63:5823–5833, (2023).